Identifying the Manipulation of Individual Atomic-Scale Defects for Boosting Thermoelectric Performances in Artificially Controlled Bi_2Te_3 Films

Min Zhang,[1] Wei Liu,[1,*] Cheng Zhang,[1] Sen Xie,[1,2] Zhi Li,[1] Fuqiang Hua,[1,2] Jiangfan Luo,[1] Zhaohui Wang,[1,2] Wei Wang,[1] Fan Yan,[1] Yu Cao,[1] Yong Liu,[3] Ziyu Wang,[4] Ctirad Uher,[5] Xinfeng Tang,[1,*]

[1]State Key Laboratory of Advanced Technology for Materials Synthesis and Processing, Wuhan University of Technology, Wuhan 430070, China

[2]International School of Materials Science and Engineering, Wuhan University of Technology, Wuhan 430070, China

[3]School of Physics and Technology, and the Key Laboratory of Artificial Micro/Nano structures of Ministry of Education, Wuhan University, Wuhan 430072, China

[4]The Institute of Technological Sciences, Wuhan University, Wuhan 430072, China

[5]Department of Physics, University of Michigan, Ann Arbor, Michigan 48109, United States

Corresponding Emails: w.liu@whut.edu.cn, tangxf@whut.edu.cn

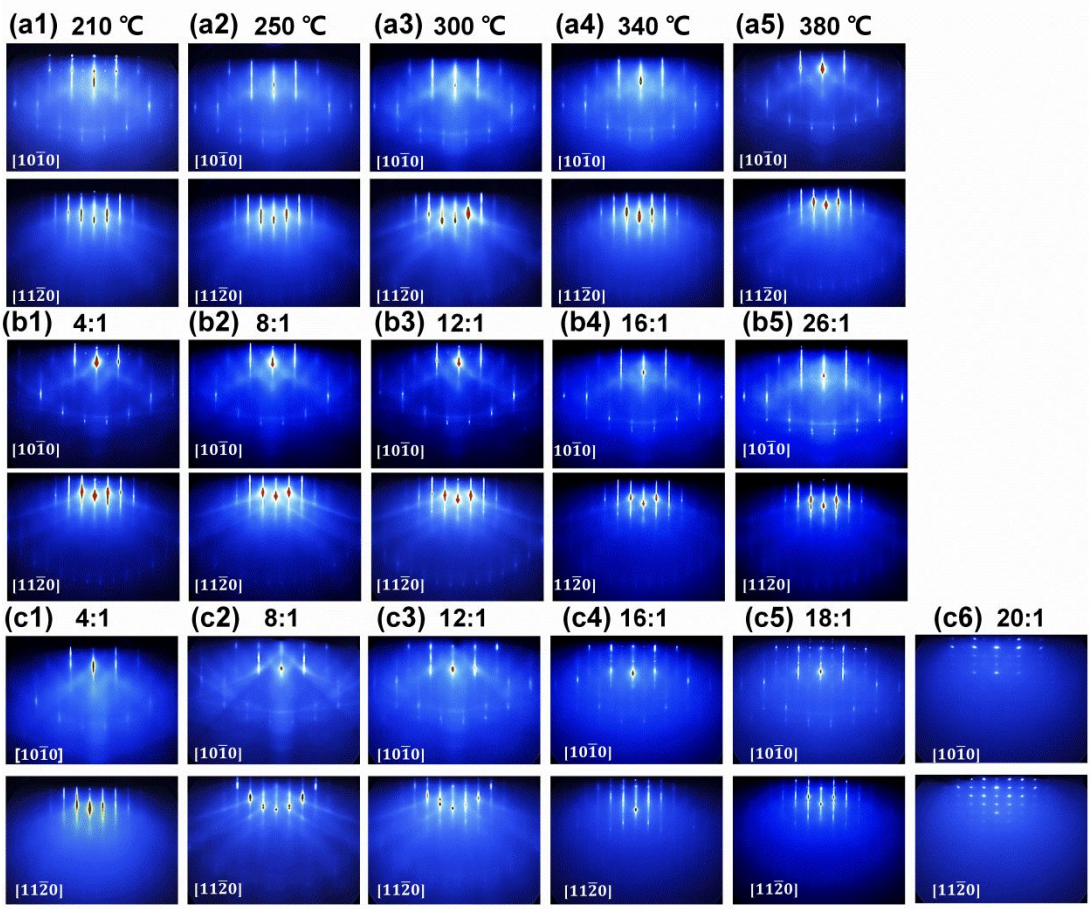

Figure S1. RHEED patterns along $[10\bar{1}0]$ and $[11\bar{2}0]$ azimuthal directions for Bi_2Te_3 films grown at different substrate temperatures T_{sub} and Te/Bi flux ratios R. (a1-a5): R = 4 and T_{sub} = 210 °C (a1), 250 °C (a2), 300 °C (a3), 340 °C (a4), and 380 °C (a5); (b1-b5): T_{sub} = 300 °C and R = 4:1 (b1), 8:1 (b2), 12:1 (b3), 16:1 (b4), and 26:1 (b5); T_{sub} = 250 °C and R = 4:1 (c1), 8:1 (c2), 12:1 (c3), 16:1 (c4), 18:1 (c5), and 20:1 (c6). Well-defined and sharp RHEED streaks along the $[10\bar{1}0]$ and $[11\bar{2}0]$ azimuthal directions reveal the single crystalline nature of the MBE grown Bi_2Te_3 films. The crystallinity of Bi_2Te_3 films grown at lower T_{sub} and higher R becomes poor, which is evident from the transition of streaky patterns to spotty patterns, as shown in (c5) and (c6).

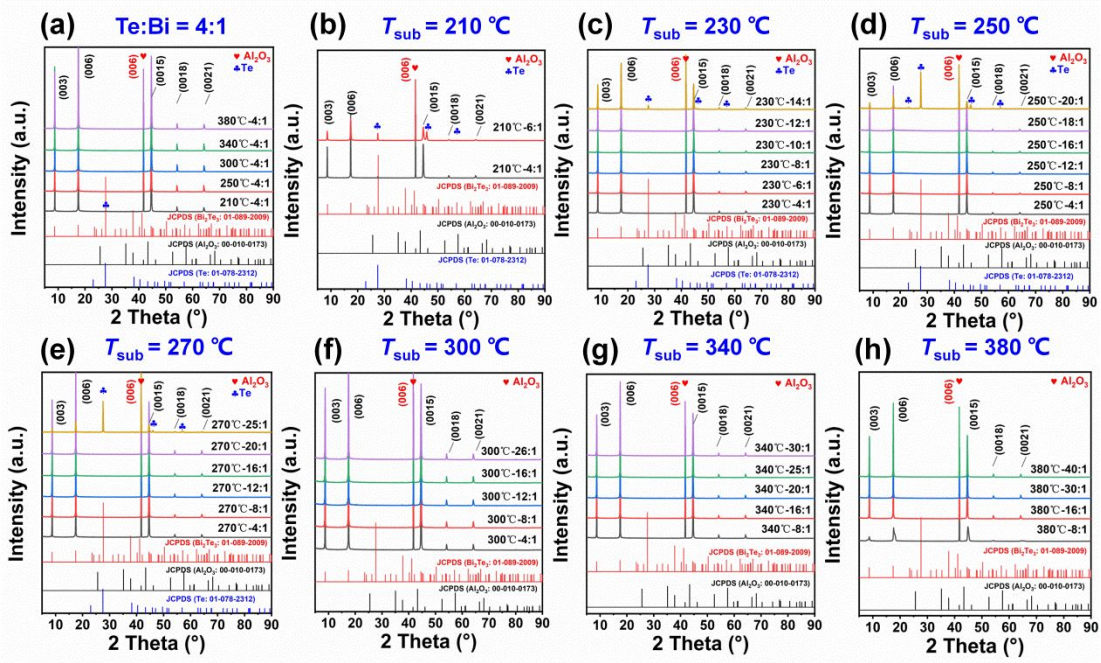

Figure S2. XRD patterns of Bi_2Te_3 films grown at different T_{sub} and R: R = 4/1 and T_{sub} = 210 ~ 380 °C (a); T_{sub} = 210 °C and R = 4/1 and 6/1 (b); T_{sub} = 230 °C and R = 4/1 ~ 14/1 (c); T_{sub} = 250 °C and R = 4/1 ~ 20/1 (d); T_{sub} = 270 °C and R = 4/1 ~ 25/1 (e); T_{sub} = 300 °C and R = 4/1 ~ 26/1 (f); T_{sub} = 340 °C and R = 8/1 ~ 30/1 (g); T_{sub} = 380 °C and R = 4/1 ~ 40/1 (h). We observe obvious extra peaks, which could be indexed to Te precipitates, in Bi_2Te_3 films grown at T_{sub} = 210 °C and R = 6/1, T_{sub} = 230 °C and R = 14/1, T_{sub} = 250 °C and R = 20/1 as well as T_{sub} = 270 °C and R = 25/1, respectively, which is due to the excess of Te. For other Bi_2Te_3 films, except for the peak at ~42 ° originating from the sapphire substrate, all other diffraction peaks can be indexed to the standard (00*l*) patterns of Bi_2Te_3, verifying their (00*l*) single crystal characteristics.

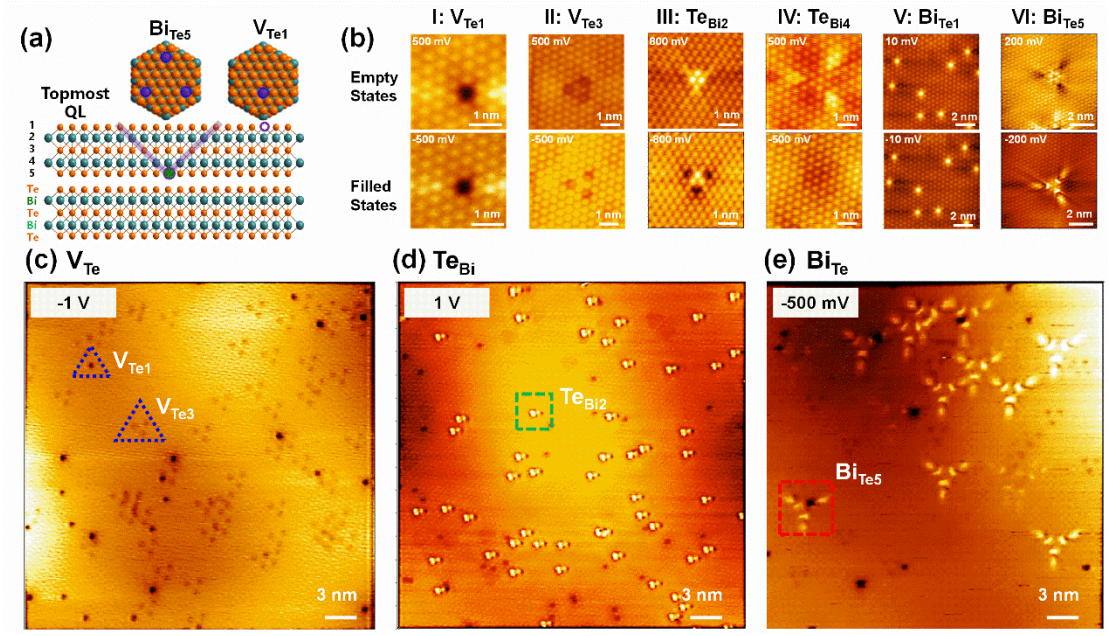

Figure S3. (a) Schematic diagram of the stacked quintuple layers for Bi_2Te_3 and the STM surface topographies of point defects; (b) High resolution STM surface topographies of different intrinsic point defects in Bi_2Te_3 films at the negative bias (filled states) and at the positive bias (empty states), respectively: (I) V_{Te1} - dark holes, (II) V_{Te3} - dark triangles, (III) Te_{Bi2} - bright and dark triangles, (IV) Te_{Bi4} - bright trefoil and dark triangle, (V) Bi_{Te1} - bright spots, and (VI) Bi_{Te5} – depressed and bright double triangles. The STM images (30 nm × 30 nm) of Bi_2Te_3 films with the different dominant surface point defects of V_{Te} (c), Te_{Bi} (d) and Bi_{Te} (e) grown at T_{sub} = 250 °C and R = 4/1, T_{sub} = 250 °C and R = 12/1 as well as T_{sub} = 300 °C and R = 4/1, respectively. In (a), the lateral numbers of 1 to 5 indicate the Nth atomic layers in the topmost QL.

In Bi_2Te_3, the STM surface morphology of intrinsic point defects is the projection of the local electron density of states of the defects onto the outermost Te layer,[1] which is intimately related to the type of defects, their locations in the QL, the in-plane threefold symmetry, and the coordination characteristics of Bi and Te. The Te vacancy on the first atomic layer, denoted as V_{Te1}, appears as a vacant site with a significant depression at positive or negative sample bias. Similar to V_{Te1}, the Te vacancy at the third atomic layer (V_{Te3}) forms a dark triangular shape morphology. As for the STM topography on a flat surface, the donor-like point defect will exhibit a bright protrusion while the acceptor-like point defect will present a dark depression at

the negative sample bias.[2,3] The opposite image contrast will be observed at the positive sample bias. Thus, the antisites Te_{Bi2} and Te_{Bi4}, as Te occupies the sites of Bi at the second and fourth atomic layer, show a bright triangular and a bright trefoil shape structure, respectively, at positive sample bias, and show dark triangular regions at negative sample bias, verifying that they are electron donors. In addition, the antisites Bi_{Te} appear chiefly at the first and fifth atomic layer, marked as Bi_{Te1} and Bi_{Te5}, respectively. The Bi_{Te1} defect always shows a bright spot at negative or positive sample bias[2,3] owing to the much larger atomic radius of Bi than Te. The Bi_{Te5} defect exhibits a depressed and a bright double-triangle morphology at the positive and negative bias, respectively, implying their acceptor nature.

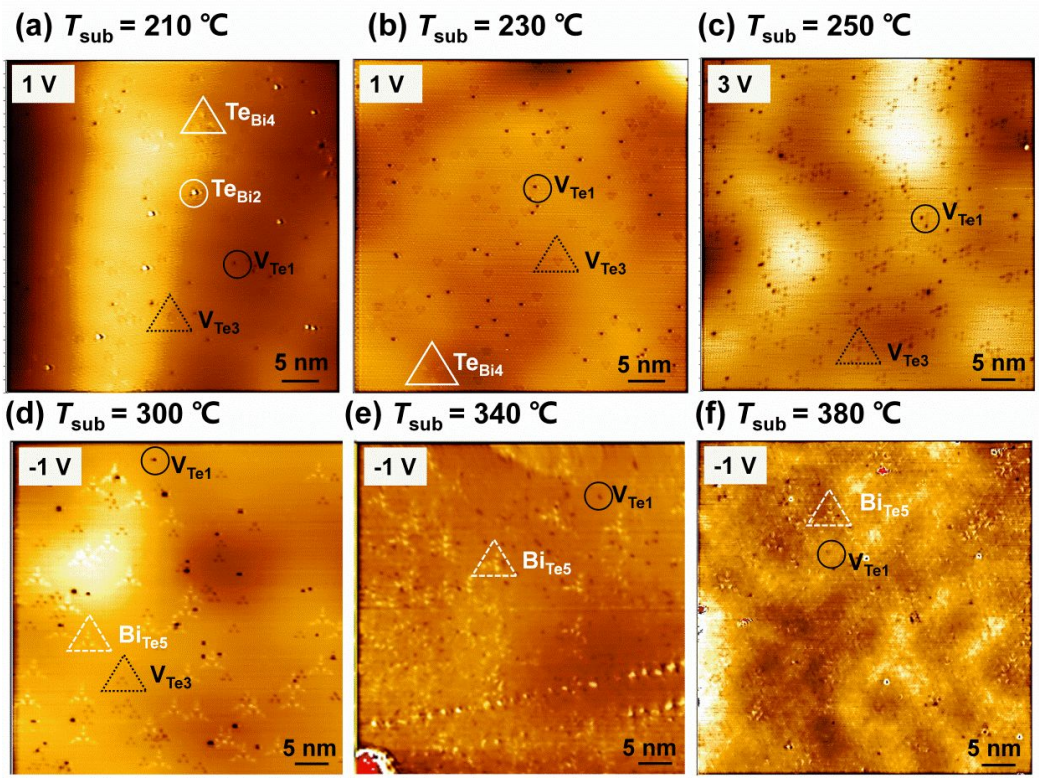

Figure S4. STM images (50 nm × 50 nm) of Bi_2Te_3 films grown at R = 4/1 and T_{sub} = 210 °C (a), 230 °C (b), 250 °C (c), 300 °C (d), 340 °C (e), and 380 °C (f). Higher T_{sub} will result in a more serious re-evaporation of Te, and thus obviously facilitate the formation of vacancies V_{Te} and Bi_{Te} antisites as well as their *in-situ* transformation $V_{Te} \rightarrow Bi_{Te}$.

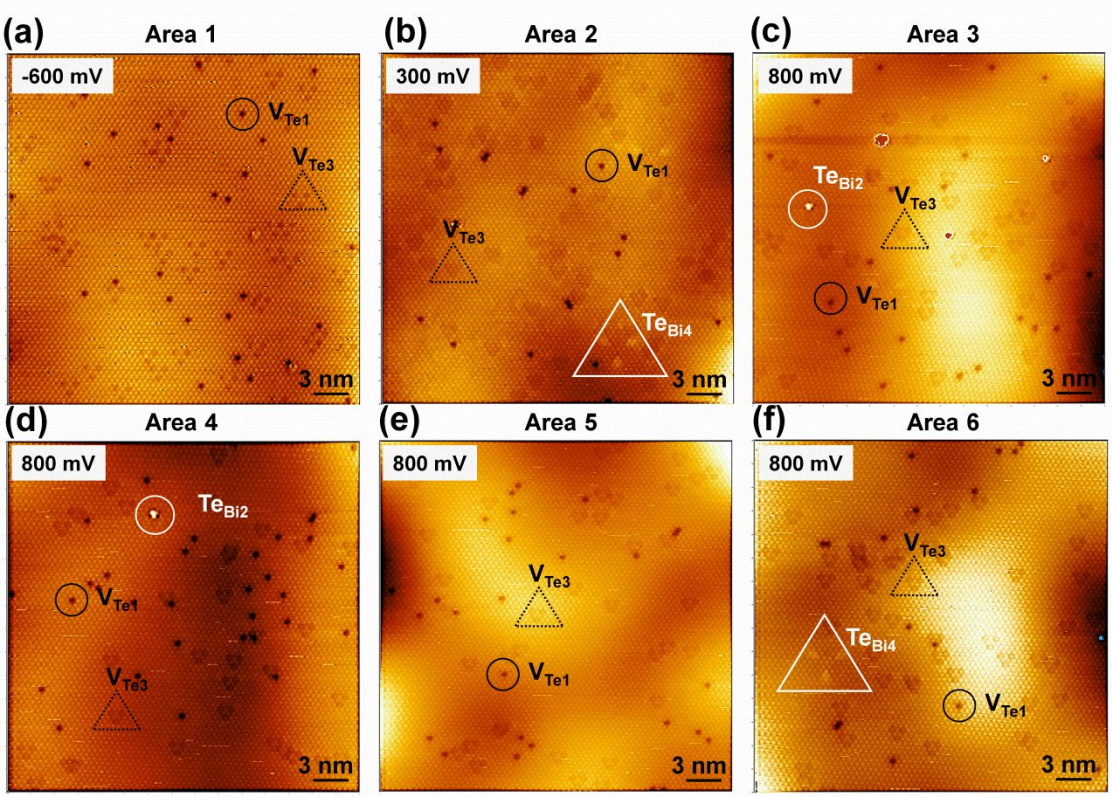

Figure S5. STM images from different areas of the Bi_2Te_3 film grown at T_{sub} = 230 °C and R = 4/1. Six large-area (30 nm × 30 nm) STM images show similar features of the point defects, which contain dominant vacancies V_{Te} and also a minority of Te_{Bi} antisites.

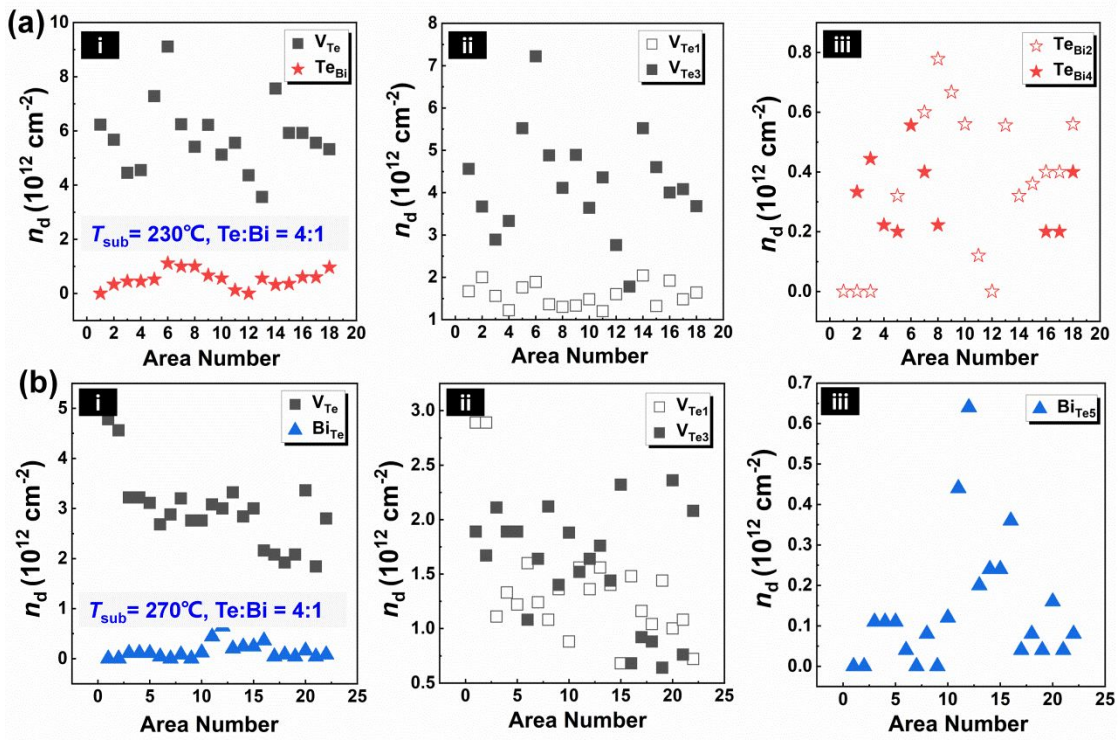

Figure S6. Statistical analysis of the density of surface point defects in different areas of Bi_2Te_3 films grown at (a) T_{sub} = 230 °C and R = 4/1 as well as (b) T_{sub} = 270 °C and R = 4/1

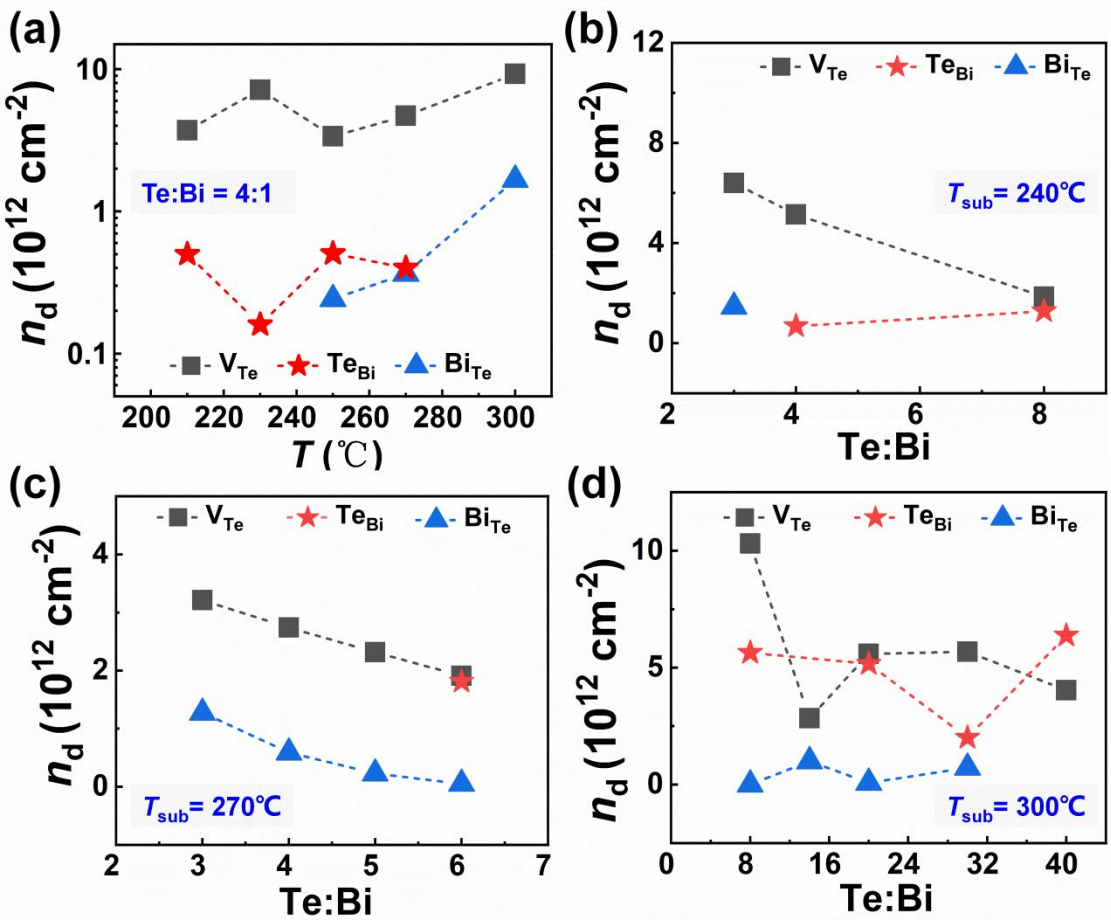

Figure S7. The summary of the surface defect density for Bi_2Te_3 films grown at different T_{sub} and R: R = 4/1 and T_{sub} = 210 ~ 300 °C (a); T_{sub} = 240 °C and R = 3/1 ~ 8/1 (b); T_{sub} = 270 °C and R = 3/1 ~ 6/1 (c); T_{sub} = 300 °C and R = 8/1 ~ 40/1 (d). The data are summarized based on the statistical analysis in various measurement areas, as shown in Figs. S4 and S5.

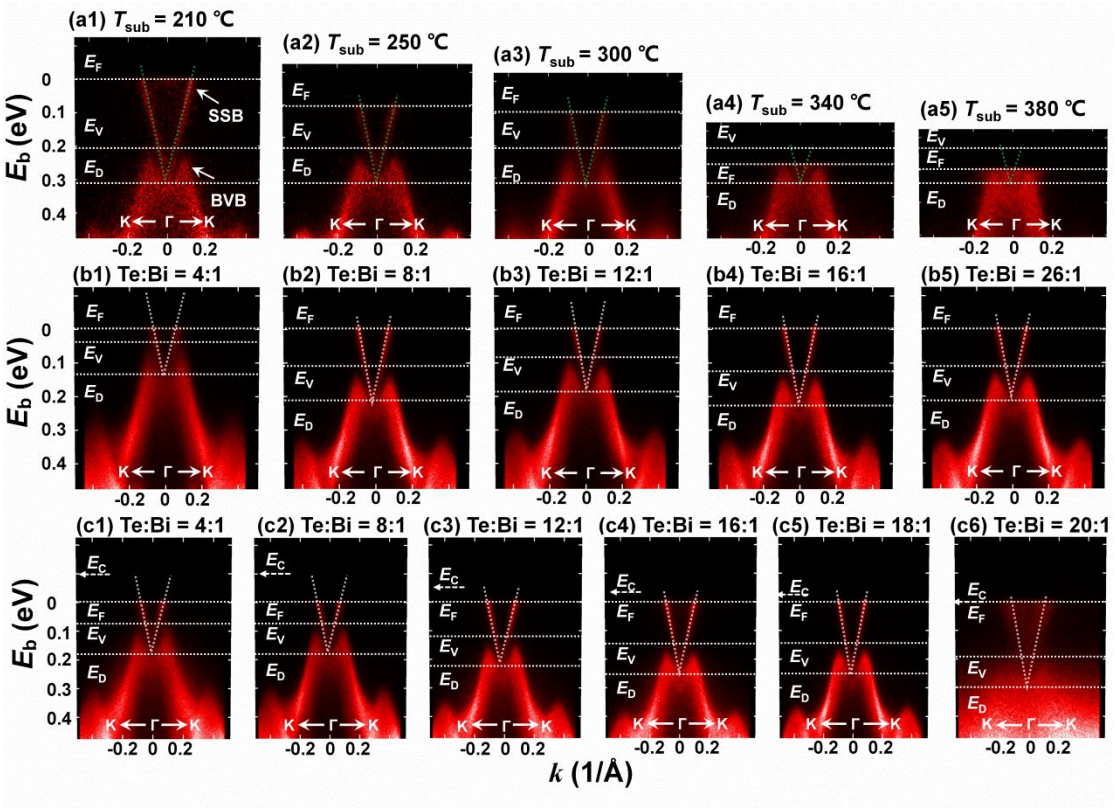

Figure S8. The ARPES electronic band structures along the Γ-K direction measured at 10 K for Bi_2Te_3 films grown at various T_{sub} and R. (a1-a5): R = 4 and T_{sub} = 210 °C (a1), 250 °C (a2), 300 °C (a3), 340 °C (a4), and 380 °C (a5); (b1-b5): T_{sub} = 300 °C and R = 4:1 (b1), 8:1 (b2), 12:1 (b3), 16:1 (b4), and 26:1 (b5); T_{sub} = 250 °C and R = 4:1 (c1), 8:1 (c2), 12:1 (c3), 16:1 (c4), 18:1 (c5), and 20:1 (c6). The E_D, E_v, E_c and E_F are the energy positions of the Dirac point, the valence band maximum, the conduction band minimum and the Fermi level, while BVB and SSB represent the bulk valence band and the surface state band, respectively. With increasing the T_{sub} from 210 °C to 380 °C, an obvious downshift of the E_F(ARPES) is observed for Bi_2Te_3 films, due to the increased density of p-Bi_{Te} defects. In addition, with increasing the R value, the E_F(ARPES) of Bi_2Te_3 films gradually moves towards the conduction band due to the increased density of n-Te_{Bi} defects.

Table S1: Room temperature physical parameters of Bi_2Te_3 films grown at different T_{sub} and R. (d stands for the film thickness, D is the grain size, n_H is the electron density, μ is the carrier mobility, σ is the electrical conductivity, S is the Seebeck coefficient, PF is the power factor, m^* stands for carrier effective mass and l is the mean free path of electrons) The positive S is found in the Bi_2Te_3 films grown at R = 4/1 as well as at T_{sub} = 340 °C and 380 °C, indicating the p-Bi_{Te} defects dominate the electronic transport. The grain size D and the mean free path l are calculated similarly as in references 4–6.

T	Te:	d	D	n_H	μ	σ	S	PF	m^*	l
℃	Bi	nm	nm	10^{19} cm^{-3}	cm^2 V^{-1} s^{-1}	10^4 S m^{-1}	μV K^{-1}	mW m^{-1} K^{-2}	m_e	nm
210	4:1	138	81	4.0	55	3.5	-210	1.5	1.2	4.3
250	4:1	125	112	5.9	30	2.9	-127	0.5	1.0	2.2
300	4:1	122	112	6.4	25	2.3	-149	0.5	1.1	1.9
340	4:1	108	85	9.6	36	5.6	3	0.0006	\	\
380	4:1	98	84	47.2	7	5.3	9	0.004	\	\
210	4:1	60	81	8.6	71	9.7	-182	3.23	1.8	6.8
210	6:1	175	132	4.8	32	2.3	-104	0.25	0.7	1.8
230	4:1	67	97	4.5	40	2.9	-137	0.54	0.9	2.7
230	6:1	53	104	5.5	53	4.7	-190	1.70	1.4	4.5
230	8:1	66	85	8.3	63	8.4	-186	2.93	1.8	6.1
230	10:1	67	85	8.9	66	9.4	-210	4.14	2.1	6.9
230	12:1	66	161	4.9	53	4.1	-198	1.61	1.3	4.4
240	4:1	84	85	4.7	43	3.2	-125	0.49	0.8	2.8
240	8:1	85	91	4.0	67	4.3	-175	1.32	1.1	4.9
240	12:1	87	145	4.0	67	4.3	-216	2.02	1.3	5.4
240	14:1	94	130	5.1	59	4.8	-220	2.33	1.5	5.2
240	16:1	95	112	7.3	82	9.5	-189	3.39	1.6	7.5
240	16:1	210	97	5.4	90	7.7	-209	3.38	1.5	7.9
250	4:1	62	66	3.9	78	4.8	-160	1.23	1.0	5.3
250	8:1	63	85	6.2	63	6.2	-165	1.70	1.1	5.0
250	12:1	67	90	7.0	70	7.9	-163	2.10	1.4	6.0
250	16:1	68	104	8.2	87	9.8	-183	3.26	1.7	8.2
250	18:1	68	85	11.1	81	14.4	-180	4.66	2.1	8.4
250	20:1	71	66	15.0	46	11.0	-161	2.86	2.3	5.0

Table S2: Room temperature physical parameters of Bi_2Te_3 films grown at different T_{sub} and R. The positive S of the Bi_2Te_3 film grown at T_{sub} = 270 °C and R = 30:1 is caused by the presence of p-Te precipitates in the matrix as in references 7-8.

T	Te:Bi	d	D	n_H	μ	σ	S	PF	m^*	l
℃		nm	nm	10^{19} cm^{-3}	cm^2 V^{-1} s^{-1}	10^4 S m^{-1}	μV K^{-1}	mW m^{-1} K^{-2}	m_e	nm
270	4:1	54	76	8.4	31	4.16	-124	0.62	1.2	2.4
270	8:1	60	85	6.9	39	4.36	-147	0.94	1.2	3.2
270	12:1	62	76	7.2	35	4.0	-128	0.67	1.1	2.6
270	16:1	67	85	7.9	31	3.98	-167	1.11	1.5	2.8
270	20:1	60	97	8.0	50	6.4	-194	2.42	1.7	4.8
270	25:1	72	69	6.4	38	3.89	-91	0.30	0.7	2.3
270	30:1	263	85	4.2	15	1.02	15	0.0023	/	/
300	4:1	59	63	12.4	26	5.1	-112	0.64	1.4	2.2
300	8:1	58	104	10.2	21	3.4	-149	0.76	1.6	1.9
300	16:1	61	69	7.0	44	4.9	-135	0.89	1.1	3.3
300	20:1	77	91	5.9	47	4.4	-131	0.75	1.0	3.4
300	26:1	63	63	6.2	49	4.9	-162	1.28	1.3	4.0
340	8:1	59	104	42.6	5	3.40	-31	0.03	0.9	0.3
340	16:1	61	112	8.1	28	3.61	-135	0.66	1.3	2.3
340	20:1	48	85	7.6	41	5.1	-151	1.17	1.3	3.5
340	25:1	62	104	8.4	26	3.56	-118	0.50	1.1	2.0
340	30:1	64	104	8.5	27	3.65	-134	0.66	1.3	2.2
380	8:1	42	50	97.2	13	19.8	-69	0.93	3.4	1.7
380	16:1	58	132	10.7	23	3.99	-115	0.53	1.3	1.9
380	30:1	54	91	13.9	17	3.75	-31	0.04	0.4	0.8
380	40:1	62	81	9.8	23	3.59	-72	0.19	0.8	1.4

Table S3: Room temperature σ, S and PF of Bi_2Te_3 films grown at T_{sub} = 250 °C with different R, measured by the PPMS and ZEM-3 apparatus. The deviation from two measurements is within ± 10%, majorly due to the measurement uncertainty from two different testing equipments.

T	Te:Bi	From PPMS			From ZEM-3		
℃		σ	S	PF	σ	S	PF
		10^4 S m^{-1}	μV K^{-1}	mW m^{-1} K^{-2}	10^4 S m^{-1}	μV K^{-1}	mW m^{-1} K^{-2}
250	4:1	4.8	-160	1.23	4.0	-152	0.92
250	8:1	6.2	-165	1.70	4.2	-164	1.13
250	12:1	7.9	-163	2.10	6.6	-173	1.97
250	16:1	9.8	-183	3.26	8.9	-191	3.25
250	18:1	14.4	-180	4.66	12.8	-186	4.43
250	20:1	11.0	-161	2.86	10.1	-162	2.65

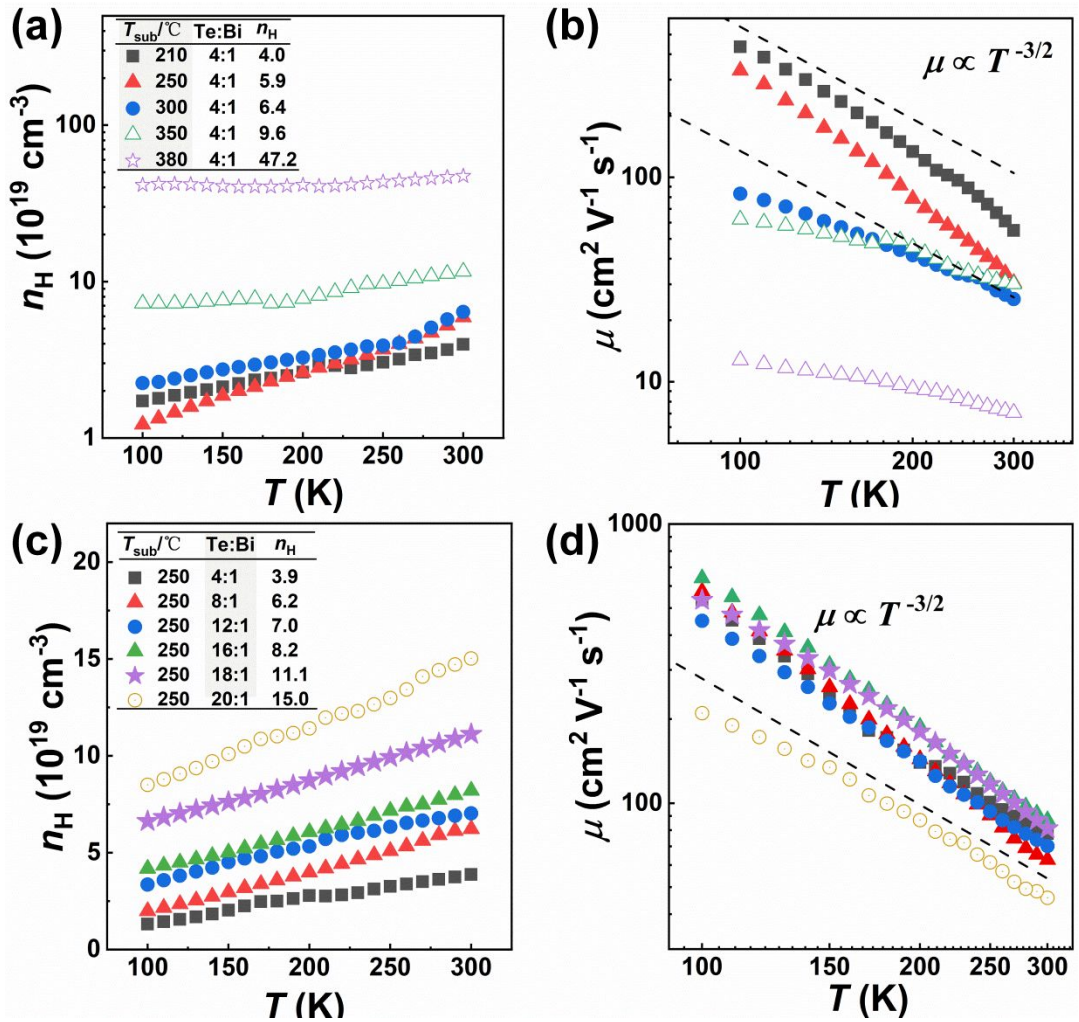

Figure S9. (a-b) Temperature dependence of n_H and μ of the Bi_2Te_3 films grown at R = 4/1 and T_{sub} = 210 ~ 380 °C; (c-d) Temperature dependence of n_H and μ of the Bi_2Te_3 films grown at T_{sub} = 250 °C and R = 4/1 ~ 20/1.

The n_H rises sharply with the increasing temperature, which suggests the formation of shallow donor levels near the conduction band minimum associated with the intrinsic point defects.[6,9] The mobility μ follows the $T^{-3/2}$ dependence, which suggests that the acoustic phonon scattering becomes the dominant carrier scattering mechanism at room temperature.[10]

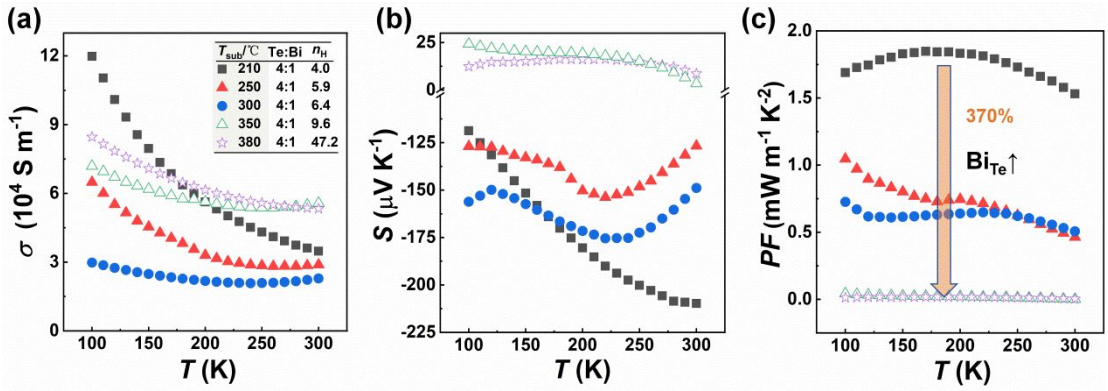

Figure S10. Temperature dependence of σ, S and PF of the Bi_2Te_3 films grown at R = 4/1 and T_{sub} = 210 ~ 380 ºC.

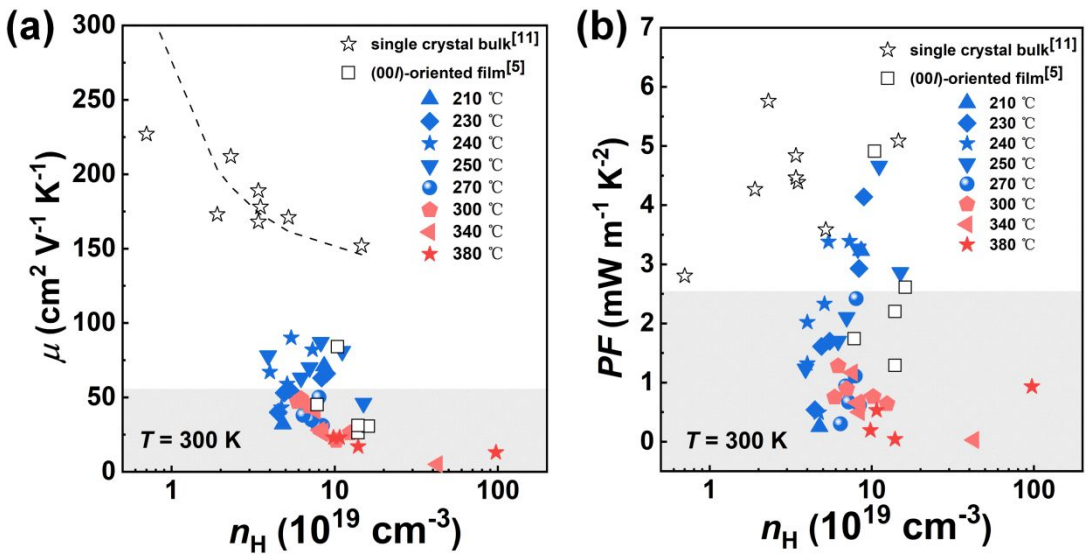

Figure S11. (a) The dependence of the carrier mobility μ on the carrier concentration n_H and (b) the dependence of the power factor PF on the carrier concentration n_H in n-Bi_2Te_3 films at room temperature. The literature data for single crystal bulks and films are included for comparison.

References:

(1) Jiang, Y.; Sun, Y. Y.; Chen, M.; Wang, Y.; Li, Z.; Song, C.; He, K.; Wang, L.; Chen, X.; Xue, Q. K.; Ma, X.; Zhang, S. B. Fermi-Level Tuning of Epitaxial Sb_2Te_3 Thin Films on Graphene by Regulating Intrinsic Defects and Substrate Transfer Doping. *Phys. Rev. Lett.* **2012**, *108* (6), 1–5.

(2) Netsou, A.; Muzychenko, D. A.; Dausy, H.; Chen, T.; Song, F.; Schouteden, K.; Van Bael, M. J.; Van Haesendonck, C. Identifying Native Point Defects in the Topological Insulator Bi_2Te_3. *ACS Nano* **2020**, *14* (10), 13172–13179.

(3) Bathon, T.; Achilli, S.; Sessi, P.; Golyashov, V. A.; Kokh, K. A.; Tereshchenko, O. E.; Bode, M. Experimental Realization of a Topological *P-N* Junction by Intrinsic Defect Grading. *Adv. Mater.* **2016**, *28* (11), 2183–2188.

(4) Goncalves, L. M.; Couto, C.; Alpuim, P.; Rolo, A. G.; Völklein, F.; Correia, J. H. Optimization of Thermoelectric Properties on Bi_2Te_3 Thin Films Deposited by Thermal Co-Evaporation. *Thin Solid Films* **2010**, *518* (10), 2816–2821.

(5) Wu, Z.; Mu, E.; Che, Z.; Liu, Y.; Sun, F.; Wang, X.; Hu, Z. Nanoporous (00*l*)-Oriented Bi_2Te_3 Nanoplate Film for Improved Thermoelectric Performance. *J. Alloys Compd.* **2020**, *828*, 154239.

(6) Zhang, M.; Liu, W.; Zhang, C.; Qiu, J.; Xie, S.; Hua, F.; Cao, Y.; Li, Z.; Xie, H.; Uher, C.; Tang, X. Thickness-Dependent Electronic Transport Induced by *in Situ* Transformation of Point Defects in MBE-Grown Bi_2Te_3 Thin Films. *Appl. Phys. Lett.* **2020**, *117* (15), 153902.

(7) Lin, S.; Li, W.; Chen, Z.; Shen, J.; Ge, B.; Pei, Y. Tellurium as a High-Performance Elemental Thermoelectric. *Nat. Commun.* **2016**, *7*, 1–6.

(8) Qian, X.; Xiao, Y.; Zheng, L.; Qin, B.; Zhou, Y.; Pei, Y.; Yuan, B.; Gong, S.; Zhao, L. D. Effective Dopants in *P*-Elementary Te Thermoelectrics. *RSC Adv.* **2017**, *7* (29), 17682–17688.

(9) Huang, B.; Lawrence, C.; Gross, A.; Hwang, G. S.; Ghafouri, N.; Lee, S. W.; Kim, H.; Li, C. P.; Uher, C.; Najafi, K.; Kaviany, M. Low-Temperature Characterization and Micropatterning of Coevaporated Bi_2Te_3 and Sb_2Te_3 Films. *J. Appl. Phys.* **2008**, *104* (11), 1–9.

(10) Zhang, M.; Zhang, C.; You, Y.; Xie, H.; Chi, H.; Sun, Y.; Liu, W.; Su, X.; Yan, Y.; Tang, X.; Uher, C. Electron Density Optimization and the Anisotropic Thermoelectric Properties of Ti Self-Intercalated $Ti_{1+X}S_2$ Compounds. *ACS Appl. Mater. Interfaces* **2018**, *10* (38), 32344–32354.

(11) Satterthwaite, C. B.; Ure, R. W. Electrical and Thermal Properties of Bi_2Te_3. *Phys. Rev.* **1957**, *108* (5), 1164–1170.